A Mock Implementation of Fused LEO GNSS

Samuel C. Morgan*, Zacharias M. Komodromos†, Wenkai Qin†, Zachary L. Clements*,
Andrew Graff‡,W. Jeremy Morrison*, Todd E. Humphreys*
*Department of Aerospace Engineering and Engineering Mechanics, The University of Texas at Austin
†Department of Electrical and Computer Engineering, The University of Texas at Austin
‡CesiumAstro

***Abstract*—This paper presents the first experimental demonstration of fused low Earth orbit (LEO) GNSS using pseudorange measurements, achieved through a mock implementation that distributes orbit and clock models as if supplied by the constellation operator. Obtaining resilient and accurate position, navigation, and timing (PNT) from broadband LEO constellations is a topic of vigorous ongoing research. Such constellations offer key advantages over traditional GNSS: proliferated satellite coverage, high power, wideband signals, and the potential for near-zero age-of-data clock and orbit models. SpaceX's expanding Starlink constellation and known frame structure make it an especially compelling candidate for LEO PNT. But recent analysis of its downlink frame timing and its published orbits indicates that stand-alone opportunistic use of Starlink signals (i.e., without cooperation from Starlink nor access to accurate third-party models) could not provide pseudorange-based PNT competitive in performance with traditional GNSS. By contrast, a fused LEO GNSS approach in which Starlink supplies real-time clock and orbit corrections to subscribers, offers a promising pathway to accurate PNT despite frame timing irregularities. This study develops downlink-beam-specific parameterized orbit and clock models tailored to Starlink's frame clock variations. Then, as if from the constellation operator in a hypothetical fused LEO GNSS service, these models are distributed to users who combine them with live-signal Starlink observables to produce navigation and timing solutions with 10-meter-level accuracy. These results demonstrate that fused LEO GNSS is a viable alternative or complement to traditional GNSS for moderately accurate and resilient PNT.**

***Index Terms*—Starlink, positioning, low Earth orbit, fused LEO GNSS**

I. Introduction

High data throughput has quickly become the standard for enabling high-quality video streaming, efficient remote work, and realistic low-latency extended and augmented reality, among other applications. Until recently, these capabilities were limited to areas with existing infrastructure or significant financial investment in new infrastructure. The advent of low Earth orbit (LEO) mega-constellation broadband networks has expanded these capabilities globally.

To achieve high data throughput and serve multiple users, large signal bandwidths are required. Interestingly, these large bandwidths inherently enable highly accurate time of arrival (TOA) measurements, which are critical for positioning, navigation, and timing (PNT) services. However, current LEO broadband networks such as SpaceX's Starlink and Eutelsat's OneWeb have yet to fully capitalize on this advantage by offering PNT services to their users. While Starlink offers a Starlink positioning mode for their user terminals, it is far from mature, often taking several minutes to achieve a low-resolution position solution [1]. Moreover, it is not a service offered directly to users, but is instead only an internal mechanism to support a user terminal's initial network entry.

The use of LEO constellations for PNT is already well-studied in the literature [2], [3]. They offer an attractive complement or backup to GNSS amid rising threats of GNSS jamming and spoofing [4]–[8]. Broadly, four primary approaches have been identified. Table I summarizes each approach in terms of deployment costs, availability, accuracy, time to fix, and dependency on traditional GNSS. References [9] and [10] give an overview of several dedicated LEO PNT projects, while the authors in [11] develop one of the first receivers for such a constellation—Xona Space Systems' Pulsar. The fused LEO GNSS concept of operations is explored in [12] and [13], and methods for extracting high-quality TOA measurements using existing communications infrastructure within a fused LEO GNSS paradigm are presented in [14] and [15].

Two recent examples of network-aided opportunistic LEO PNT based on Doppler measurements are presented in [17] and [18], with promising positioning results. In [17], a mobile rover is aided by a reference station with known position. This approach additionally requires GNSS timing for initialization. The authors of [18] performed simulations along with two field experiments. In their first experiment, they eliminated satellite vehicle (SV) clock and ephemeris errors by using the same receiver for both the reference and the rover. In their second experiment, a 635-km baseline separated the reference and rover, implying they received signals from different Starlink beams. As reported in [26], significant frame and frame-rate offsets exist from beam to beam, but whatever carrier Doppler offsets were present appear not to have prevented a useful positioning solution.

Note that Table I also classifies the opportunistic approach presented in [16] as network-aided because the receiver being tracked is aided by GNSS signals during an initialization phase, which allows estimation of LEO satellite ephemeris, clock, and clock rate errors just as occurs with network aiding. In effect, the receiver acts as its own reference station during the initialization phase, holding over key estimated values during the GNSS-denied phase.

The authors in [19] present another network-aided opportunistic approach using the Iridium constellation. They set up nearly-zero and short baselines between their reference and rover receivers, then perform positioning using time difference of arrival and frequency difference of arrival. But their PNT solutions attain only modest accuracy due to Iridium's narrow bandwidth, which limits TOA measurement resolution.

Preprint of the 2025 IEEE/ION Position, Location, and Navigation Symposium (PLANS), Salt Lake City, UT, April 28-May 1, 2025

TABLE I: LEO PNT Trade Space

	Dedicated [9]–[11]	Fused [12]–[15]	Network-Aided Opportunistic [16]–[20]	Stand-Alone Opportunistic [21]–[25]
Description	LEO constellation or hosted payloads dedicated solely to PNT.	Fuses a secondary PNT service with a primary communications service.	Like stand-alone opportunistic, but a network of reference stations provides corrections.	Exploits unmodified signals from communications SVs. Public ephemerides. No network aiding.
Marginal deployment cost	high: constellation of SVs	low: uses communications hardware and signals	high: network of reference stations	very low
Potential availability	mid-term	near-term	near-term for local coverage	immediate
Potential accuracy [m]	< 1	< 1	< 1	< 100
Time to fix [s]	< 10	< 10	< 10	< 1000
Dependency on traditional GNSS	@SVs in near-term	@SVs in near-term	@reference stations in near-term	@SVs in some cases

In [20] the authors implement a similar approach using the OneWeb constellation. They envision a third-party network-aided opportunistic approach in which the reference stations provide clock and orbit models as a form of differential corrections. Due to OneWeb's wide bandwidth signal, they achieve good PNT accuracy despite poor-quality ephemerides.

Notably, the overwhelming majority of opportunistic LEO PNT methods presented in the literature are Doppler-based [27]. But compared to pseudorange-based PNT techniques, Doppler-based techniques have worse timing accuracy by many orders of magnitude (milliseconds vs. nanoseconds), even under optimistic measurement noise and satellite clock offset rate assumptions [22], [24], [28]. Recognizing that many PNT applications of practical interest require accurate timing, we focus on pseudorange-based PNT, or PNT based on TOA measurements.

Among current LEO broadband providers, Starlink holds the greatest potential for highly accurate pseudorange-based LEO PNT. Up to 16 Starlink beams may be directed to a single service cell, providing favorable instantaneous geometry. Additionally, Starlink's wide bandwidth signals ($F_s = 240\,\mathrm{MHz}$) contain deterministic pilot sequences that enable extremely accurate TOA measurements [26], [29], [30]. In fact, Starlink's extraordinary bandwidth provides far more resistance to multipath than the widest traditional GNSS signal, the 51.15-MHz Galileo E5 AltBOC signal. Moreover, the Starlink signal does not suffer from the the side-peak ambiguity problem inherent in Galileo AltBOC processing [31].

Stand-alone opportunistic pseudorange-based PNT with Starlink appears intractable due to onboard clocks exhibiting inconsistent, unmodelable behavior [26]. Therefore, we look to a network-aided opportunistic or fused approach for this paper's pseudorange-based PNT formulation, aiming for meter-accurate positioning and nanosecond-accurate timing.

Given that timing errors for Starlink SVs are in the worst case beam-specific [26], a network-aided opportunistic PNT solution would be especially costly: the inter-station spacing for the reference network would need to be smaller than the Starlink beam diameter, or approximately 20 km. Thus, a fused communications-and-PNT solution, as advocated in [12], appears more favorable for the Starlink constellation. Nonetheless, a fused solution may be simulated with a network-aided opportunistic solution: The same corrections to ephemeris and timing models, together with pilot symbols for greater detection sensitivity and improved TOA and Doppler measurement precision, can be sent to a user receiver by the reference network as if it had been sent by the Starlink network itself. Thus, a network-aided opportunistic implementation amounts to a mock fused implementation.

In this paper we propose treating the Starlink constellation as though it were a fully operational fused LEO GNSS. This approach involves two receivers, a reference station, designated as the control segment (CS), and a user receiver, designated as the customer terminal (CT). The CS functions as a ground station, equipped with a high-gain antenna and a high-quality clock. It monitors SVs transmitting to its service cell and gathers key information, including transmission timestamps, SV clock errors, and data symbols. Using these observations along with its known position, the CS derives accurate clock and orbital models, which it then relays to the CT as if sent within the data message of transmitting Starlink SVs. The CT, in turn, uses this information to form pseudorange measurements and compensate for SV clock errors in its PNT solution.

The CT is assumed to be a consumer-grade device that, in the worst case, operates with a low-gain omnidirectional antenna, a low-quality clock, and a narrow-bandwidth front-end. Under these conditions, it may receive signals in a low signal-to-noise ratio (SNR) regime, making it difficult to extract TOA measurements using the known pilot sequences alone. To mitigate this, the CS may designate additional pilot sequences beyond those used for communications. These additional pilots would enhance TOA measurement accuracy, even in low SNR conditions. However, such data resources would not be allocated arbitrarily for two reasons. First, improper selection could introduce errors due to high sidelobes in the autocorrelation function of the pilot-bearing downlink signal. Second, any allocation of symbols as pilots prevents their use

as conveyors of data, cutting into downlink data rate capacity. Instead, a select few data resources are chosen optimally to minimize the Ziv-Zakai bound (ZZB) as described in [14].

We implement the proposed approach in a field campaign. CS and CT receivers are used to simultaneously record data within the same Starlink service cell. The recorded data are processed as described, and a PNT solution is determined using nonlinear batched least squares (NBLS). The resulting solution achieves 10-meter-level accuracy despite suboptimal capture bandwidth and ephemeris errors, providing motivation for two further developments: (1) the implementation of a dedicated fused LEO GNSS service (as discussed in [12]), or (2) the establishment of a third-party service that deploys reference stations in key service cells, offering the necessary information to client receivers for opportunistic navigation with the Starlink signal, as discussed in [10].

The rest of this paper is organized as follows. In Section II, we present the system concept of operations and its relation to our mock implementation. Section III discusses the Starlink Ku-band downlink signal structure and defines relevant terminology. In Section IV, we present the necessary SV and receiver clock model. Section V enumerates three potential data-aiding strategies to improve TOA measurement accuracy. In Section VI, we explain how the CS provides ephemeris and clock corrections. The estimator used to produce a PNT solution is developed in Section VII. Section VIII describes our specific experiment and presents the PNT results. Finally, Section IX, provides some further insights about the work.

II. Concept of Operations

This section outlines the key assumptions underlying the fused LEO GNSS concept as regards the CS, the SV constellation, and the CT. It then provides a brief overview of this paper's experiment and explains how each component aligns with the established assumptions.

A. Fused LEO GNSS

We assume a constellation of SVs primarily dedicated to providing broadband internet to its users, with a secondary mission to offer PNT services at minimal additional cost to the user and minimal opportunity cost (i.e., reduced throughput) to the communications service. This dual-purpose system, referred to as fused LEO GNSS in [12], will be referred to as such throughout this paper. Additionally, GNSS as we know them (i.e., GPS, Galileo, Beidou, etc.) will be referred to as traditional GNSS from this point forward.

A fused LEO GNSS could elect to rely on traditional onboard GNSS receivers to perform orbit determination and clock disciplining. However, this approach subjects itself to all the weaknesses that a fused LEO GNSS seeks to overcome. That is, service would be denied when traditional GNSS would be denied. It is worth mentioning that despite this key flaw, using traditional onboard GNSS receivers could be a near-term solution for existing constellations such as Starlink and OneWeb as there is nearly no deployment cost.

In the long term, in a fused LEO GNSS, a network of ground stations is essential to perform precise orbit determination and clock monitoring of the constellation. This network of ground stations, referred to as the CS, provides ephemeris and clock corrections to the SVs, which are then disseminated to end users.

The constellation of SVs may operate in a transparent or regenerative scheme. They may transmit a waveform of any type, across any number of frequency channels, at varying levels of directionality, and using any polarization desired by the service provider to ensure sufficient orthogonality.

The constellation is assumed to operate in LEO and to be a so-called mega-constellation. A mega-constellation consists of a large number of SVs, ranging from a few hundred (e.g., Eutelsat's Oneweb) to several thousand (e.g., SpaceX's Starlink). Constellations of this size are crucial as they provide broad communications coverage and excellent geometric diversity for PNT.

The CT is assumed to be a consumer device capable of engaging in whatever resource allocation scheme the network has employed. For example, if the network's constellation of SVs transmits narrow beams across multiple frequency channels, the CT is assumed to be equipped with a phased array antenna capable of receiving the highly-directional beams and rapidly switching between them as scheduled, along with the necessary radio frequency (RF) chains to process signals at any of the frequency channels.

It is not necessary for every CT to decode all the data transmitted by a given SV. Data destined for other users are assumed to be encrypted and thereby inaccessible to a given CT.

If the CT is designated for PNT, it need only be capable of computing a PNT solution using the network resources allocated for PNT services. This opens the possibility for a distinct category of CT: the PNT-only device. Since the signal-to-noise ratio (SNR) requirements for PNT are significantly lower than those for broadband communication, a service provider could feasibly offer a compact, portable PNT-only CT with a low-gain, possibly omnidirectional, antenna. However, even a PNT-only CT would still require sufficient bandwidth to precisely measure TOA using pilot symbols.

B. Mock Implementation

Since no fused LEO GNSS constellation is yet deployed, we develop an experimental demonstration of the concept via a mock implementation, with Starlink as our target constellation. Our mock implementation retains all essential elements of the fused approach.

In our implementation, the CS consists of a single reference station at a known position, mounted on the roof of the parking garage adjoining the Aerospace Engineering Building at the University of Texas. Equipped with a high-gain antenna, the CS is capable of receiving full-bandwidth (F_s =240 MHz) Ku-band downlink signal data from a single Starlink SV at a time. By processing the digitized received signal, augmented with knowledge of its own position, access to precise GPS time (GPST), and atmospheric models, the CS provides differential corrections to the CT.

Our implementation's CT is assumed to be PNT-only and is situated at a location unknown to the CS. Specifically,

the CT comprises a low-gain antenna and an RF front-end capable of capturing only a 25-MHz real-time bandwidth—a small fraction of the total bandwidth of Starlink Ku-band downlink waveform. The CT is also limited to receiving data on a single frequency channel at a time. This configuration represents a pessimistic scenario, as the CT cannot reliably and accurately measure TOAs based solely on existing Starlink pilot sequences that support communications, such as the PSS and the SSS revealed in [29]. Instead, it must be fed additional pilot data by the CS to overcome weak SNR by additional processing gain.

Moreover, since the CS only tracks and produces corrections for a single SV at a time, the CT is unable to compute a single-epoch pseudorange-based PNT solution, as is possible with traditional GNSS. Instead, it emulates single-epoch PNT by tracking a sequence of Starlink SVs with an RF front-end driven by a highly stable receiver clock so that it need only estimate a single receiver clock offset and a single clock offset rate, as would be the case for a single-epoch solution.

III. Signal Structure

This section introduces the Starlink frame structure, drawn from [29], and additional concepts and terminology needed to understand Starlink operation in general and Starlink-based PNT in particular.

A. Frame Structure

As shown in Fig. 1, each Starlink downlink orthogonal frequency division multiplexing (OFDM) frame consists of 302 intervals of length $T_{\text{sym}} = 4.4\,\mu\text{s}$ plus a frame guard interval T_{fg}, for a total frame period of $T_{\text{f}} = 1/F_{\text{f}}$ s, where $F_{\text{f}} = 750$ Hz is the frame rate. Each frame begins with the primary synchronization sequence (PSS), which is natively represented in the time domain, followed by the secondary synchronization sequence (SSS), which is formatted as a standard 4PSK OFDM symbol. The final occupied symbol interval in each frame is the coda symbol, which is followed by the frame guard interval. Subsequent frames may be present or not, depending on user demand.

The time-domain modulation sequence of the PSS, and the frequency-domain symbol sequence of the SSS were revealed in [29]. These sequences allow a Starlink receiver to perform the channel estimation necessary to demodulate each OFDM symbol in the frame. In particular, the PSS allows the receiver to precisely identify the beginning of each frame, while the SSS allows it to perform equalization across all subcarriers. The PSS and SSS have a fixed phase relationship, which allows coherent integration across the combined PSS + SSS interval, permitting more accurate synchronization and carrier frequency offset (CFO) estimation, as shown in [26].

B. Assigned Beams

At any given time, a user within Starlink's $\pm 53°$ latitude primary coverage area may have a direct line of sight to dozens of overhead SVs above $20°$ elevation [12]. Each Starlink SV is capable of simultaneously directing up to 48 downlink beams to terrestrial service cells, 16 for each of its three downlink phased arrays. A proprietary beam assignment procedure assigns each beam to a ∼20-km-diameter service cell [32]. A service cell may be illuminated by up to 16 beams simultaneously, two beams for each of the eight frequency channels identified in [29]. We call the $N_{\text{b}i}$ beams deliberately directed to the ith service cell *assigned beams*.

The number of distinct SVs casting assigned beams onto the ith service cell, $N_{\text{as}i} \leq N_{\text{b}i} \leq 16$, may be less than $N_{\text{b}i}$ because a given SV may project multiple beams onto the same cell, each on a different channel or with a different polarization (right-hand vs. left-hand circular polarization). As Starlink user density has increased over the past few years, $N_{\text{as}i}$ and $N_{\text{b}i}$ have generally increased. It was shown in [33] that a search procedure prioritizing high-elevation SVs was effective at finding multiple illuminating SVs.

C. Fixed Assignment Interval

Several publications have noted the existence of a 15-s Starlink network reconfiguration interval [33]–[36]. Because all beam assignments remain fixed over the duration of this interval, we call it the *fixed assignment interval* (FAI). FAI boundaries appear to be approximately aligned with GPST [33]. As discussed in [26], noticeable transitions in Starlink frame timing behavior occur at FAI boundaries.

IV. Clock Models

This section introduces the Starlink clock models described in [26]. These models will be necessary to derive the clock corrections provided by the CS in Section VI.

A. Beam-Specific Clock Cascade Model

Fig. 2 presents a clock cascade model for a single Starlink downlink beam. The model is beam-specific because, as shown in [26], frame timing behavior may differ from beam to beam over the same FAI for the same SV. This remarkable observation implies that Starlink signal timing is much different from that of traditional GNSS, in which a single clock governs the whole transmission cascade across all frequencies. To be sure, in traditional GNSS timing offsets may be present between different spreading codes on the same carrier and across multiple carriers, resulting in so-called differential code biases [37]. But the code rates as transmitted are all a constant multiple of a single base clock's reference frequency. By contrast, the frame sequences on different beams from the same Starlink SV may differ in both time offset and rate, a fact with significant implications for Starlink-based PNT.

The root of each clock cascade is a base oscillator. As shown in [26], this oscillator is shared across all beams from a given SV. An onboard GNSS receiver driven by the base oscillator produces a clock disciplining signal s_{d} that corrects the base oscillator towards GPST. Together, the base oscillator and the GNSS receiver form a closed feedback loop that produces the GNSS-disciplined timing signal t_{d}.

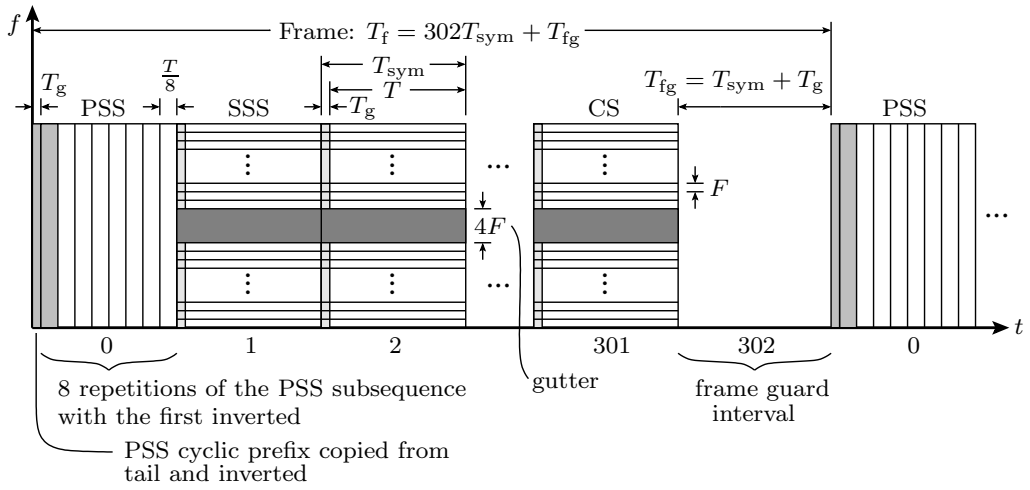

Fig. 1: Frame layout for the Ku-band Starlink downlink along time-frequency dimensions, from [29]. Indices along the horizontal axis enumerate the 303 intervals that constitute a single frame. The quantity T is the useful (non-cyclic) OFDM symbol interval, T_g is the symbol guard interval (cyclic prefix), and F is the subcarrier spacing. Other quantities are defined in the text.

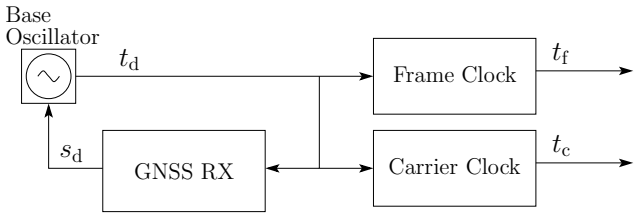

Fig. 2: Clock cascade model for a single Starlink downlink beam, from [26].

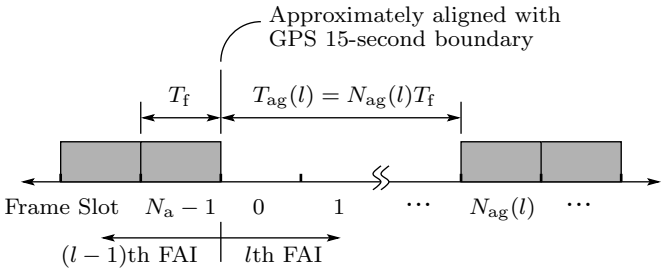

Fig. 3: Frame sequence timing diagram showing the transition from the $(l-1)$th FAI to the lth FAI.

B. Frame and Carrier Clocks

The GNSS-disciplined timing signal t_d drives the frame and carrier clocks. In turn, the frame clock's signal t_f governs the timing of frames transmitted by the SV, and the carrier clock's signal t_c drives the carrier onto which the information-bearing frames are modulated. The frame clock is likely a software-based clock whose output t_f depends on when baseband frames are loaded into buffers for mixing to RF and subsequent transmission. The carrier clock is likely transparent, meaning that $t_\mathrm{c} = t_\mathrm{d}$, but it is represented in a manner identical to the frame clock for full model generality.

Note that in traditional GNSS the clock driving each SV's spreading code (analogous to the frame clock) also drives the underlying carrier that the spreading code modulates [38]. Thus, the code and the carrier—as transmitted—are locked together such that the code chipping rate is a constant rational multiple of the carrier frequency. In the case of Starlink downlink signals, the frame and carrier clocks operate somewhat independently, which is why they are represented separately in Fig. 2 [26].

We represent frame and carrier clock offsets from t_d as Δt_f and Δt_c. These are related to t_d, t_f, and t_c by

$$t_\mathrm{d}(t) = t_\mathrm{f}(t) - \Delta t_\mathrm{f}(t) \quad (1)$$
$$t_\mathrm{d}(t) = t_\mathrm{c}(t) - \Delta t_\mathrm{c}(t) \quad (2)$$

where t represents true time, or time according to an ideal clock, such as is closely realized by GPST [39]. In this paper, true time and GPST are taken to be synonymous. The frame and carrier clocks are related to t by

$$t = t_\mathrm{f}(t) - \delta t_\mathrm{f}(t) \quad (3)$$
$$t = t_\mathrm{c}(t) - \delta t_\mathrm{c}(t) \quad (4)$$

where $\delta t_\mathrm{f}(t)$ and $\delta t_\mathrm{c}(t)$ are the frame and carrier clock offsets.

The time derivatives of $\delta t_\mathrm{f}(t)$ and of $\delta t_\mathrm{c}(t)$ are called the frame and carrier clock drift. They are equivalent to the instantaneous fractional frequency deviation, written generically as $y(t)$, on which clock stability analysis is based [40].

C. Discrete-Time Frame Clock

The frame sequence timing diagram in Fig. 3 offers further details about the frame clock. Each frame as transmitted has a duration of exactly T_f according to the frame clock. Within each FAI, the frame slot index increments from 0 to $N_\mathrm{a} - 1$, with $N_\mathrm{a} = 11250$ being the number of frame slots in one FAI. Each FAI starts at the beginning of frame slot 0 and lasts $N_\mathrm{a}T_\mathrm{f} = 15\,\mathrm{s}$. The interval of unoccupied frame slots at the beginning of the lth FAI, called the FAI guard interval $T_\mathrm{ag}(l) = N_\mathrm{ag}(l)T_\mathrm{f}$, spans a variable number of frame slots $N_\mathrm{ag}(l)$. Note

that, for any FAI index l, frame slot $N_{\text{ag}}(l)$ is occupied by definition, but other frame slots may not be occupied.

Let $t_{\text{f}}(i,l,m)$ be the frame clock time for the ith Starlink SV at the instant when the frame in the mth frame slot of the lth FAI begins to pass through the phase center of the SV's downlink antenna, where l and m are zero-based indices. By definition, we take this to be

$$t_{\text{f}}(i,l,m) \triangleq 15l + mT_{\text{f}} \tag{5}$$

Let $t^*(i,l,m)$ and $\delta t_{\text{f}}(i,l,m)$ be the corresponding GPST and frame clock offset. Then

$$t^*(i,l,m) = t_{\text{f}}(i,l,m) - \delta t_{\text{f}}(i,l,m) \tag{6}$$

D. Receiver Clock

Now consider the clock of a receiver (e.g., the CT) tracking signals from the Starlink downlink. The receiver clock time t_{r} is related to true time t by

$$t = t_{\text{r}}(t) - \delta t_{\text{r}}(t_{\text{r}}) \tag{7}$$

The receiver clock offset $\delta t_{\text{r}}(t_{\text{r}})$ is represented as a function of t_{r} because it is natively ordered in receiver time in the course of solving for a position and time solution. The time derivative of δt_{r} with respect to t, denoted $\dot{\delta t}_{\text{r}}(t_{\text{r}}(t))$, is called the receiver clock drift.

Let $t_{\text{r}}(i,l,m)$ be the time of reception, according to the receiver clock, of the frame transmitted by the ith SV at true time $t^*(i,l,m)$. Let $\delta t_{\text{r}}(i,l,m)$ be the corresponding receiver clock offset and $t_*(i,l,m)$ be the corresponding true time of reception. More precisely, $t_{\text{r}}(i,l,m)$ is the receiver clock time at which the frame transmitted at true time $t^*(l,m)$ from the ith SV's downlink antenna's phase center first reached the receiver antenna's phase center. The receipt time $t_{\text{r}}(i,l,m)$ can be related to $t_*(i,l,m), t^*(i,l,m)$, and $t_{\text{f}}(i,l,m)$ by

$$t_*(i,l,m) = t_{\text{r}}(i,l,m) - \delta t_{\text{r}}(i,l,m) \tag{8}$$

$$t^*(i,l,m) = t_{\text{r}}(i,l,m) - \delta t_{\text{r}}(i,l,m) - \delta t_{\text{tof}}(i,l,m) \tag{9}$$

$$\begin{aligned} t_{\text{f}}(i,l,m) = {} & t_{\text{r}}(i,l,m) - \delta t_{\text{r}}(i,l,m) - \delta t_{\text{tof}}(i,l,m) \\ & + \delta t_{\text{f}}(i,l,m) \end{aligned} \tag{10}$$

where $\delta t_{\text{tof}}(i,l,m)$ is the frame's time of flight from transmission to reception, expressed as an interval in true time.

V. Data Aiding

The inclusion of additional pilot sequences in the local replica generated by the CT improves both detection and TOA measurement performance. This section discusses three data-aiding strategies that affect the CT's processing gain: (1) no data aiding: the CT only uses the PSS and SSS (PSS+SSS); (2) using the PSS, SSS, and optimally allocated subcarrier pilots, according to the ZZB (Optimal Pilots); and (3) using the entire data frame within the CT's front-end bandwidth as the local replica, either decoded by the CT or allocated by the CS (Full Frame).

A. PSS + SSS

Given that the CT can detect the Starlink signal using a local replica of the PSS + SSS alone, TOA measurements obtained this way should provide reasonable accuracy. In [26], the authors show that sub-centimeter accuracy is theoretically achievable at moderate SNR with full bandwidth. Since our implemented CT is limited to only 25 MHz of bandwidth, a new calculation is necessary. A lower bound on TOA error variance for a signal with Fourier transform $S(f)$, energy E, and noise spectral density N_0 can be expressed by [41, Eq.11.15]

$$\sigma_\tau^2 \geq \frac{1}{2\gamma^2 \frac{E}{N_0}} \tag{11}$$

where γ^2 is the effective squared bandwidth defined as

$$\gamma^2 \triangleq \frac{\int_{-\infty}^{\infty} (2\pi f)^2 |S(f)|^2 df}{\int_{-\infty}^{\infty} |S(f)|^2 df}. \tag{12}$$

The PSS signal given in [29, Eq. 34] has a Fourier transform

$$S_{\text{PSS}}(f) \triangleq \frac{1}{F_{\text{s}}} \sum_{k=-N_{\text{g}}}^{N-1} \text{rect}\left(\tfrac{f}{F_{\text{s}}}\right) \exp\left(-j2\pi(k+N_{\text{g}})\tfrac{f}{F_{\text{s}}}\right) p_k \tag{13}$$

and, when sampled at 25 MHz, an effective bandwidth of $\gamma_{\text{PSS}} = 3.9977 \times 10^7$ Hz. Similarly, the SSS signal given in [29, Eq. 1.37] has a Fourier transform

$$S_{\text{SSS}}(f) \triangleq \sum_{k=-\frac{N}{2}}^{\frac{N}{2}-1} X_{m1k} \exp\left(-j2\pi F T_{\text{g}} k\right) G_{\text{s}}(f - Fk) \tag{14}$$

$$G_{\text{s}}(f) \triangleq \mathscr{F}[g_{\text{s}}(t)] = T_{\text{sym}} \text{sinc}\left(T_{\text{sym}} f\right) \exp\left(-j\pi T_{\text{sym}} f\right) \tag{15}$$

and, when sampled at 25 MHz, an effective bandwidth of $\gamma_{\text{SSS}} = 4.6063 \times 10^7$ Hz. The PSS and SSS signal combined in a single frame have a Fourier transform of $S_1(f) = S_{\text{PSS}}(f) + \exp\left(-j2\pi T_{\text{sym}} f\right) S_{\text{SSS}}(f)$ and when sampled at 25 MHz, an effective bandwidth of $\gamma_{\text{PSS+SSS}} = 4.3283 \times 10^7$ Hz. Importantly, if the PSS + SSS can be used to form a TOA measurement, the network would incur no loss of data capacity.

B. Optimal Pilots

Due to the low received SNR at the CT, the CS may transmit demodulated data from the Starlink frame to the CT. The CT can then correlate these data resources in addition to the already-known synchronization sequences, allowing for a more accurate TOA estimate than would be achievable with the PSS and SSS alone. This technique can be considered as a form of data aiding in our experiment. In practice, however, the Starlink network would designate these data resources as known pilots, and the CT would have *a priori* knowledge of them.

In this scheme, it is critical that the overhead required to transmit this data to the CT is minimized, ensuring reliable and low-latency data transmission. To achieve this, the CT

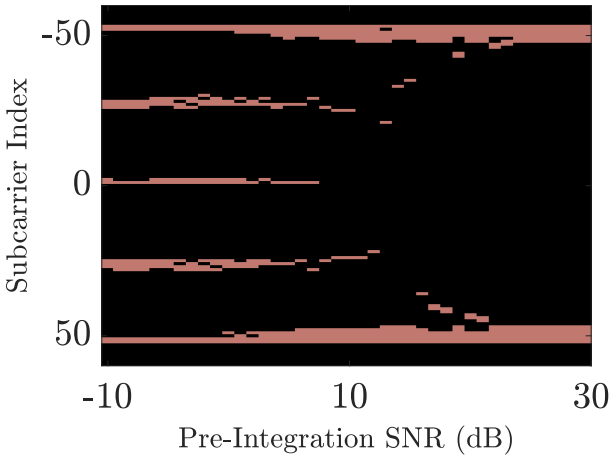

Fig. 4: The optimized selections of 12 out of 106 available subcarriers for data aiding as a function of pre-integration SNR.

receives only a small selection of demodulated data resources corresponding to a sparse subset of subcarriers that span the CT's available bandwidth. However, the specific selection of subcarriers will affect the TOA autocorrelation function. If the CT is provided with a suboptimal allocation, its autocorrelation function may exhibit ambiguities or high sidelobe levels, leading to misdetections and increased TOA estimation errors. Conversely, if the CT is provided an optimal allocation, the autocorrelation function will exhibit a sharp mainlobe and adequately suppressed sidelobes, improving the TOA accuracy for the given SNR.

Using the noncoherent integer-constrained ZZB-minimization techniques from [14], an optimized set of subcarrier selections was generated for pre-integration SNRs ranging from $-10\,\mathrm{dB}$ to $30\,\mathrm{dB}$. In this minimization, the ZZB assumed an *a priori* TOA window with a duration equal to that of the cyclic prefix. The returned allocations are near-optimal, achieving a ZZB TOA variance within $5\,\%$ of the true optimal selection. Each selection consists of 12 out of 106 available subcarriers within the CT's $25\,\mathrm{MHz}$ bandwidth. These subcarrier selections are shown in Fig. 4. At low SNR, the selection is more evenly distributed across the available bandwidth, while at high SNR, the selection favors the extremities of the band, thereby maximizing the mean-squared bandwidth.

The CS can then select subcarriers based on the CT's SNR, demodulate all data resources in the Starlink frame corresponding to these subcarriers, and transmit the decoded data to the CT as though they were pilots sent by the network. If the Starlink network were to implement this, the transmitting SV would need to sacrifice 12 subcarriers per OFDM symbol in each frame. Given that each Starlink OFDM symbol consists of 1024 subcarriers, the absolute data rate loss for the entire frame would be $1.17\,\%$.

To compute a lower bound on TOA measurement errors, the Fourier transform of the entire frame at a given post-integration SNR can be described by $S_{\mathrm{O}} = S_1(f) + \sum_{k=2}^{300} \exp\left(-j2\pi k T_{\mathrm{sym}} f\right) S_{\mathrm{S}}(f)$, where $S_{\mathrm{S}}(f)$ represents the optimal subcarrier allocation for a given symbol at a specific SNR. Assuming that the SNR remains constant over the course of a frame, we can compute S_{O} for each SNR, determine the effective bandwidth, and calculate the bound on TOA accuracy.

It should be noted that these allocations are optimal on a per-symbol basis. In other words, a TOA measurement computed using a single optimal subcarrier allocation across the entire frame may not necessarily be optimal. For the purposes of this paper, we assume that the difference will be marginal. However, we acknowledge that the potential for an optimal allocation throughout the entire frame warrants further investigation in future work.

C. Full Frame

Finally, the CT may use the entire frame it has access to in order to form a TOA measurement. This could happen in two ways. In the first, the network provider may choose to dedicate the entire bandwidth of the CT to pilot subcarriers. This would mean that the CT would be designated as PNT-only, as there would no longer be data to decode. In this case, the SV would allocate 106 subcarriers per symbol per frame, assuming a CT with $25\,\mathrm{MHz}$ bandwidth. The absolute data rate loss incurred by this allocation would be $10.35\,\%$.

Alternatively, if the CT were not PNT-only, but rather had sufficient gain to permit decoding data, it could use the decoded data as a local replica to form a TOA measurement as described in [15]. This *decision-directed* scheme would incur no cost to the network, but would require a more complex CT. Additionally, any decoding errors made by the CT would affect TOA measurement accuracy.

To compute a lower bound on TOA measurement errors, we assume that the entire frame within the CT's front-end bandwidth is transmitted as pilots. The Fourier transform of the entire frame can be described by $S_{\mathrm{F}}(f) = S_1(f) + \frac{1}{F_{\mathrm{s}}} \sum_{k=2}^{300} \exp\left(-j2\pi k T_{\mathrm{sym}} f\right) \mathrm{rect}\left(\frac{f}{F_{\mathrm{s}}}\right)$, assuming that the Fourier transform of the remaining symbols in the frame is rectangular. The effective bandwidth of the entire frame under this assumption, given a limited bandwidth of $25\,\mathrm{MHz}$ is $\gamma_{\mathrm{F}} = 4.6434 \times 10^7\,\mathrm{Hz}$.

Fig. 5 plots root mean squared error (RMSE) lower bounds for the three paradigms discussed in this section over the range of $-20\,\mathrm{dB}$ to $20\,\mathrm{dB}$. The optimal pilot allocations were only optimized over a range of $-10\,\mathrm{dB}$ to $30\,\mathrm{dB}$, so the optimization for $-10\,\mathrm{dB}$ was used from $-20\,\mathrm{dB}$ to $-10\,\mathrm{dB}$ in Fig. 5. As expected, the PSS + SSS provides the worst TOA accuracy but still achieves sub-meter accuracy at relatively low SNR. Using the optimal pilot allocations results in a significant performance improvement, theoretically reaching sub-centimeter accuracy at high SNR. The use of the full frame offers the best accuracy, theoretically reaching sub-centimeter accuracy approximately 10 dB earlier than the optimal pilot configuration.

VI. Satellite Clock and Ephemeris Corrections

This section introduces the pseudorange measurement model and identifies where errors due to the ephemeris and

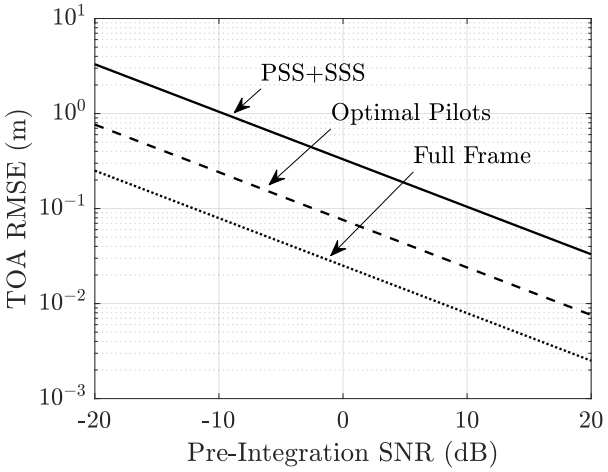

Fig. 5: TOA RMSE bounds for three levels of data aiding to a CT having a front-end bandwidth of 25 MHz. Using the PSS+SSS alone incurs no loss of data capacity, while employing 12 optimal pilot subcarriers incurs a 1.17 % loss of data capacity, and the use of the entire 25 MHz band would incur a 10.35 % loss of data capacity.

transmitter clock may arise. Additionally, we explore how these errors are mitigated in practice and in our specific experiment.

A. Pseudorange Measurement Model

In a fused LEO GNSS based on Starlink, a CT would apply (5) to obtain the time of transmission (TOT), according to the ith SV's frame clock, of the mth frame in the lth FAI. For its part, the network would send the frame clock offset $\delta t_{\mathrm{f}}(i,l,m)$ so that the CT could obtain the corresponding TOT in GPST, as in (6). Likewise, for our experiment, the frame clock offset $\delta t_{\mathrm{f}}(i,l,m)$ is estimated by the CS for provision to the CT, as described below.

Rearranging (10) to isolate $\delta t_{\mathrm{f}}(i,l,m)$ yields

$$\delta t_{\mathrm{f}}(i,l,m) = t_{\mathrm{f}}(i,l,m) - t_{\mathrm{r}}(i,l,m) + \delta t_{\mathrm{r}}(i,l,m) + \delta t_{\mathrm{tof}}(i,l,m) \tag{16}$$

If the CS can calculate, measure, or model all the quantities on the right-hand side of this equation, it will obtain an estimate of $\delta t_{\mathrm{f}}(i,l,m)$ that it can pass to the CT. To obtain $t_{\mathrm{f}}(i,l,m)$, it calculates nominal frame timing according to (5). Note that there is no ambiguity in this calculation because, as explained in [26], the CS can mark the end of a FAI by observation and count frame slots within the subsequent FAI.

The CS obtains $t_{\mathrm{r}}(i,l,m)$ by measurement. Let $\mathcal{M}_{il}$ be the set of occupied-frame indices for the lth FAI of the ith SV. A sequence of highly precise frame TOA measurements corresponding to $\mathcal{M}_{il}$ may be extracted by the CS using the maximum-likelihood (ML) methods described in [42]. For $m \in \mathcal{M}_{il}$, these are modeled as

$$\tilde{t}_{\mathrm{r}}(i,l,m) = t_{\mathrm{r}}(i,l,m) + w_{\mathrm{r}}(i,l,m) \tag{17}$$

where $w_{\mathrm{r}}(i,l,m)$ is zero-mean Gaussian measurement error with variance $\sigma_{\mathrm{r}}^2(i,l,m)$. As explained in [42], if the CS has access to the full 240-MHz channel bandwidth and an antenna with sufficient gain to provide a pre-correlation SNR of 14 dB or more, then ML TOA estimation over a full frame is remarkably precise, with range-equivalent RMSE $c\sigma_{\mathrm{r}}(i,l,m)$ less than one centimeter, where c is the speed of light in vacuum.

To obtain $\delta t_{\mathrm{r}}(i,l,m)$, the CS employs simultaneous Starlink and GNSS signal capture, accounting for all cable delays, as described in [26]. Finally, the CS models $\delta t_{\mathrm{tof}}(i,l,m)$ using meter-accurate SV ephemeris models and atmospheric models, as also described in [26].

For this paper's demonstration, meter-accurate ephemerides based on observables from a GNSS receiver onboard the Starlink SVs were not available as was the case in [26]. Instead, we were obliged to use publicly accessible Starlink ephemerides, either from space-track.org, whose ephemerides are accurate (at least periodically) to within about 10 m [43], or from NORAD-provided TLEs, which have much larger errors. Such errors caused significant errors in our modeled $\delta t_{\mathrm{tof}}(i,l,m)$. Thus, the estimated $\delta t_{\mathrm{f}}(i,l,m)$ sent from the CS to the CT, denoted $\bar{\delta t}_{\mathrm{f}}(i,l,m)$, is modeled as

$$\bar{\delta t}_{\mathrm{f}}(i,l,m) = \delta t_{\mathrm{f}}(i,l,m) + \eta(i,l,m)/c + w_{\mathrm{r}}(i,l,m) \tag{18}$$

where $\eta(i,l,m)$, given in meters and discussed further in the following subsection, is the error in $\bar{\delta t}_{\mathrm{f}}(i,l,m)$ due to ephemeris errors.

We now turn our attention to the CT, which calculates TOA just as the CS does but with a possibly reduced bandwidth and, in the case of a PNT-only CT, with ML estimation based on additional CT-provided pilot data, which provides the ML estimator a boost in processing gain to compensate for the CT's low-gain antenna. Let $\tilde{t}_{\mathrm{u}}(i,l,m)$ denote the CT's measured frame TOA for the corresponding i, l, and $m \in \mathcal{M}_{il}$, which is modeled as

$$\tilde{t}_{\mathrm{u}}(i,l,m) = t_{\mathrm{u}}(i,l,m) + w_{\mathrm{u}}(i,l,m) \tag{19}$$

where $t_{\mathrm{u}}(i,l,m)$ is the true TOA according to the CT's clock, and $w_{\mathrm{u}}(i,l,m)$ is zero-mean Gaussian measurement error with variance $\sigma_{\mathrm{u}}^2(i,l,m) \geq \sigma_{\mathrm{r}}^2(i,l,m)$. The CT's pseudorange measurement, defined as

$$\rho(i,l,m) = c\left[\tilde{t}_{\mathrm{u}}(i,l,m) - t_{\mathrm{f}}(i,l,m)\right] \tag{20}$$

may then be modeled as

$$\begin{aligned}\rho(i,l,m) = {} & r_{\mathrm{u}}(i,l,m) + c\delta t_{\mathrm{u}}(i,l,m) \\ & + \eta(i,l,m) + c\delta t_{\mathrm{atm}}(i,l,m) + w(i,l,m)\end{aligned} \tag{21}$$

where $r_{\mathrm{u}}(i,l,m)$ is the true range between the ith Starlink SV and the CT, $\delta t_{\mathrm{u}}(i,l,m)$ is the CT clock error, $\delta t_{\mathrm{atm}}(i,l,m)$ denotes atmospheric delays along the line-of-sight path, and $w(i,l,m)$ is zero-mean Gaussian measurement error with variance $c^2\left[\sigma_{\mathrm{r}}^2(i,l,m) + \sigma_{\mathrm{u}}^2(i,l,m)\right]$.

B. Ephemeris Error Modeling

If Starlink were providing PNT services as a fused LEO GNSS, the ephemeris errors would likely be low as the satellite ephemeris could be packaged in a navigation message. However, during our experiment, only TLEs were available.

As a result, it is is important to discuss the differential errors caused by the large ephemeris errors inherent in using TLEs.

At any given epoch, the position of a Starlink SV can be retrieved from publicly available TLEs. The accuracy of the SV position derived from a TLE is typically accurate to the kilometer-level. However, after 24 hours since the TLE was last updated, these spatial errors can grow to be 1 to 10 km [44]. This subsection aims to characterize how these spatial ephemeris errors affect the differential pseudorange error when measured at the CS and CT. For simplicity, we consider a single satellite, a single FAI, and a single frame, and thus omit the corresponding notation.

Let $\boldsymbol{p}_{\mathrm{s}}$ denote the true position of the SV, $\boldsymbol{p}_{\mathrm{r}}$ the known position of the CS, and $\boldsymbol{p}_{\mathrm{u}}$ the position of the CT. The true ranges between $\boldsymbol{p}_{\mathrm{r}}$ and $\boldsymbol{p}_{\mathrm{s}}$, and $\boldsymbol{p}_{\mathrm{u}}$ and $\boldsymbol{p}_{\mathrm{s}}$, are denoted r_{r} and r_{u}, respectively. These ranges are expressed as

$$r_{\mathrm{r}} = \sqrt{(\boldsymbol{p}_{\mathrm{r}} - \boldsymbol{p}_{\mathrm{s}})^{\mathsf{T}}(\boldsymbol{p}_{\mathrm{r}} - \boldsymbol{p}_{\mathrm{s}})} \tag{22}$$

$$r_{\mathrm{u}} = \sqrt{(\boldsymbol{p}_{\mathrm{u}} - \boldsymbol{p}_{\mathrm{s}})^{\mathsf{T}}(\boldsymbol{p}_{\mathrm{u}} - \boldsymbol{p}_{\mathrm{s}})} \tag{23}$$

Now, suppose that the assumed SV position contained a 3D spatial error $\boldsymbol{\epsilon}$. The resulting ranges, when assuming the erroneous SV position at the CS, $\tilde{r}_{\mathrm{r}}$, and at the CT, $\tilde{r}_{\mathrm{u}}$, are expressed as

$$\tilde{r}_{\mathrm{r}} = H_{\mathrm{r}}\boldsymbol{\epsilon} + r_{\mathrm{r}} \tag{24}$$

$$\tilde{r}_{\mathrm{u}} = H_{\mathrm{u}}\boldsymbol{\epsilon} + r_{\mathrm{u}} \tag{25}$$

where H_{r} and H_{u} are the 1×3 Jacobians with respect to the SV's position, expressed as

$$H_{\mathrm{r}} = \frac{\partial r_{\mathrm{r}}}{\partial \boldsymbol{p}_{\mathrm{s}}} = -\hat{\boldsymbol{p}}_{\mathrm{r}} = -\frac{\boldsymbol{p}_{\mathrm{r}} - \boldsymbol{p}_{\mathrm{s}}}{r_{\mathrm{r}}} \tag{26}$$

$$H_{\mathrm{u}} = \frac{\partial r_{\mathrm{u}}}{\partial \boldsymbol{p}_{\mathrm{s}}} = -\hat{\boldsymbol{p}}_{\mathrm{u}} = -\frac{\boldsymbol{p}_{\mathrm{u}} - \boldsymbol{p}_{\mathrm{s}}}{r_{\mathrm{u}}} \tag{27}$$

The pseudorange measurement error at both the CS and the CT due to the spatial errors in the SV's position will manifest differently due to differences in geometry. However, if the positions of the CS and CT are close to each other, the resulting errors will be relatively small. The relative differential pseudorange error between the CS and the CT, caused by spatial ephemeris errors, is denoted as η, and is expressed as

$$\begin{aligned}\eta &= (\tilde{r}_{\mathrm{r}} - r_{\mathrm{r}}) - (\tilde{r}_{\mathrm{u}} - r_{\mathrm{u}}) \\ &= (H_{\mathrm{r}} - H_{\mathrm{u}})\,\boldsymbol{\epsilon}\end{aligned} \tag{28}$$

For example, consider a specific $\boldsymbol{p}_{\mathrm{r}}$, $\boldsymbol{p}_{\mathrm{u}}$, $\boldsymbol{p}_{\mathrm{s}}$, and 3D satellite spatial error $\boldsymbol{\epsilon} \sim \mathcal{N}(\mathbf{0}, P_{\boldsymbol{\epsilon}})$, then

$$\eta \sim \mathcal{N}(0, \sigma_\eta^2) \tag{29}$$

with

$$\sigma_\eta^2 = (H_{\mathrm{r}} - H_{\mathrm{u}})\,P_{\boldsymbol{\epsilon}}\,(H_{\mathrm{r}} - H_{\mathrm{u}})^{\mathsf{T}}) \tag{30}$$

The distribution of η in (29) requires the knowledge of $\boldsymbol{p}_{\mathrm{u}}$ to compute the Jacobian which is required for σ_η^2 . In practice, $\boldsymbol{p}_{\mathrm{u}}$ is unknown, but the CT will have *a priori* information about $\boldsymbol{p}_{\mathrm{u}}$ relative to $\boldsymbol{p}_{\mathrm{r}}$. For instance, the CT might know that it is located within the same beam footprint as the CS. In this case, $\boldsymbol{p}_{\mathrm{u}}$ is modeled as

$$\boldsymbol{p}_{\mathrm{u}} = \boldsymbol{p}_{\mathrm{r}} + \boldsymbol{\xi} \tag{31}$$

where $\boldsymbol{\xi}$ is a 3D random offset with respect to $\boldsymbol{p}_{\mathrm{r}}$, following some distribution with covariance $P_{\boldsymbol{\xi}}$. Since $\boldsymbol{p}_{\mathrm{u}}$ is now treated a random variable, $H_{\mathrm{u}}(\boldsymbol{\xi})$ and $\sigma_\eta^2(\boldsymbol{\xi})$ also become random variables. $H_{\mathrm{u}}(\boldsymbol{\xi})$ is expressed as

$$H_{\mathrm{u}}(\boldsymbol{\xi}) = H_{\mathrm{r}} + \boldsymbol{\xi}^{\mathsf{T}} A \tag{32}$$

with

$$A^{\mathsf{T}} = \frac{\partial H_{\mathrm{r}}^{\mathsf{T}}}{\partial \boldsymbol{p}_{\mathrm{r}}} = r_{\mathrm{r}}^{-1}\left(\hat{\boldsymbol{p}}_{\mathrm{r}}\hat{\boldsymbol{p}}_{\mathrm{r}}^{\mathsf{T}} - \mathbb{I}\right) \tag{33}$$

where A is the Jacobian of H_{r} with respect to $\boldsymbol{p}_{\mathrm{r}}$. The derivation of this Jacobian can be found in [45]. Consequently, (30) is reduced to

$$\sigma_\eta^2(\boldsymbol{\xi}) = \boldsymbol{\xi}^{\mathsf{T}} A P_{\boldsymbol{\epsilon}} A^{\mathsf{T}} \boldsymbol{\xi} \tag{34}$$

Now, $\sigma_\eta^2(\boldsymbol{\xi})$ is a function of the unknown random vector $\boldsymbol{\xi}$, so solving for $\bar{\sigma}_\eta^2$ is required for modeling purposes. Note, (34) is a quadratic form, thus

$$\bar{\sigma}_\eta^2 = \mathbb{E}\left[\sigma_\eta^2(\boldsymbol{\xi})\right] = \mathrm{trace}\left(A P_{\boldsymbol{\epsilon}} A^{\mathsf{T}} P_{\boldsymbol{\xi}}\right) \tag{35}$$

Finally, the distribution of η when $\boldsymbol{p}_{\mathrm{u}}$ is unknown can be modeled as

$$\eta \sim \mathcal{N}(0, \bar{\sigma}_\eta^2). \tag{36}$$

Consider the scenario where the ephemeris error is zero-mean Gaussian in the ENU frame, with covariance matrix $P_{\boldsymbol{\epsilon}} = \sigma_{\mathrm{eph}}^2\mathbb{I}$. Also, assume that $\xi \sim \mathcal{N}(\mathbf{0}, P_{\boldsymbol{\xi}})$, where $P_{\boldsymbol{\xi}} = \mathrm{diag}\left(\sigma_{\mathrm{e}}^2, \sigma_{\mathrm{n}}^2, \sigma_{\mathrm{u}}^2\right)$, centered at the CS. The choices of σ_{eph}^2, σ_{e}^2, σ_{n}^2, and σ_{u}^2 are treated as tuning parameters. The values of σ_{e}^2, σ_{n}^2, and σ_{u}^2 depend on the assumed distance between the CS and CT.

In the case of Starlink, it is required that the CS and CT occupy the same service cell. Following this, the CT's position is modeled as Gaussian with $P_{\boldsymbol{\xi}} = \mathrm{diag}\left(3300^2, 3300^2, 50^2\right)$ centered at the CS, which puts the CT inside of a service cell 95% of the time. In this paper, σ_{eph}^2 is scaled with the age of TLE. For a TLE that is 12 hours and 24 hours old, choices of $\sigma_{\mathrm{eph}} = 2.5$ km, and $\sigma_{\mathrm{eph}} = 5$ km are conservatively used, respectively. With a typical Starlink satellite to service cell geometry, $\bar{\sigma}_\eta$ = 17.8 m for a 12-hour-old TLE, and $\bar{\sigma}_\eta$ = 35.6 m for a 24-hour-old TLE. If a CT had access to high-quality ephemeris data with $\sigma_{\mathrm{eph}} = 10$ m, then $\bar{\sigma}_\eta$ = 0.07 m, which would be negligible. Since the CS and CT are within the same service cell, a small ephemeris error would affect the pseudoranges at the CS and CT in a similar manner. The distribution of η will be further exploited in Section VII.

VII. Estimation

This section uses the measurement model derived in VI to develop a NBLS estimator for obtaining the PNT solution of the CT. The NBLS estimator introduced here is similar to the traditional GNSS NBLS estimator, with additional constraints tailored to the specific requirements of our experiment.

A. Estimator Formulation

In practice, the CT would be expected to compute an instantaneous PNT solution using pseudoranges from multiple SVs all received at nearly the same time, with little ephemeris error. This estimator could be similar to what is used in traditional GNSS. The estimator developed in this section can use measurements from multiple SVs at a time, but these measurements will not be received simultaneously and, in some cases, may be spaced minutes apart. Additionally, they will also suffer from large ephemeris errors since only TLEs were available at the time of the experiment. Appropriate design changes are made to compensate for these differences. We begin by making the simplification that, for our experiment, only one FAI is used for each satellite. Therefore, we drop the FAI index from here onward. This also implies that the set $\mathcal{M}_{il} = \mathcal{M}_i$. Then, we develop the NBLS estimator by rewriting the pseudorange measurement model in (21) as

$$\begin{aligned}\rho(i,m) = r_{\text{u}}(i,m) + c[\delta t_u(0,0) \\ + \Delta t(i,m)\delta\dot{t}_u] + \eta(i) + w(i,m)\end{aligned} \tag{37}$$

where $\Delta t(i,m)$ is the time separation between the first SV's first frame and the ith SV's mth frame in seconds, $\delta\dot{t}_u$ is the CT's clock drift, which is assumed to be constant over the course of the experiment, and $\eta(i)$ is as described in Section VI. Here, we simplify by assuming that $\eta(i)$ remains constant over all FAIs and frames for a given satellite. Then, we can define our measurement vector $\boldsymbol{z}$ for n SVs as

$$\boldsymbol{z} = \begin{bmatrix} \boldsymbol{\rho}(0) \\ \boldsymbol{\rho}(1) \\ \vdots \\ \boldsymbol{\rho}(n-1) \end{bmatrix}, \quad \boldsymbol{\rho}(i) = \begin{bmatrix} \rho(i,0) \\ \rho(i,1) \\ \vdots \end{bmatrix} \tag{38}$$

where the length of $\boldsymbol{\rho}(i)$ is the cardinality of the set of occupied frames used to determine pseudorange measurements during the ith SV's FAI, denoted by $\mathcal{M}_i$.

Next, we define the state vector. Given the nature of the current experiment and the gravity of the ephemeris errors present in $\boldsymbol{z}$, it is necessary to estimate $\eta(i)$ for each SV i. However, to limit the number of total states to be estimated, we combine the CT's clock offset with $\eta(0)$ as $\delta t_\eta = c\delta t_u(0,0) + \eta(0)$. We also define $\delta\eta(i) = \eta(i) - \eta(0)$. The measurement model may then be reformulated as

$$\begin{aligned}\rho(i,m) = r_{\text{u}}(i,m) + \delta t_\eta \\ + \delta\eta(i) + c\Delta t(i,m)\delta\dot{t}_{\text{u}} + w(i,m)\end{aligned} \tag{39}$$

Where, by inspection, $\delta\eta(0) = 0$. Then, the state vector $\boldsymbol{x}$ is given by

$$\boldsymbol{x} = \begin{bmatrix} \boldsymbol{p}_{\text{u}}^{\mathsf{T}} & \delta t_\eta & \boldsymbol{\delta\eta}^{\mathsf{T}} & c\delta\dot{t}_{\text{u}} \end{bmatrix}^{\mathsf{T}} \tag{40}$$

where $\boldsymbol{p}_{\text{u}} \in \mathbb{R}^3$ are the position states of the CT in the Earth-centered, Earth-fixed coordinate system and $\boldsymbol{\delta\eta} \in \mathbb{R}^{n-1}$ is the vector of all $\delta\eta(i), i \neq 0$. Finally, we can define the design matrix H for a single row as

$$\begin{aligned}H(i,m) &= \begin{bmatrix} \frac{\partial\rho(i,m)}{\partial \boldsymbol{p}_{\text{u}}} & \frac{\partial\rho(i,m)}{\partial\delta t_\eta} & \frac{\partial\rho(i,m)}{\partial\boldsymbol{\delta\eta}} & \frac{\partial\rho(i,m)}{\partial c\delta\dot{t}_u} \end{bmatrix} \\ &= \begin{bmatrix} \hat{\boldsymbol{p}}(i,m) & 1 & \mathbf{1}_i & \Delta t(i,m) \end{bmatrix}\end{aligned} \tag{41}$$

Where $\mathbf{1}_i \in \mathbb{R}^{n-1}$ is a vector with 1 in the ith position and zeros elsewhere. We also make the important distinction that $\mathbf{1}_0 = \mathbf{0} \in \mathbb{R}^{n-1}$, or equivalently, $\mathbf{1}_0$ is the zero vector.

B. Measurement Covariance

If all measurements were independent and identically distributed (IID), we could proceed directly to form the estimate $\hat{\boldsymbol{x}}$ with ordinary least squares. However, there are two primary factors that affect the distribution of the measurements, preventing them from being IID. First, the received SNR of the ith SV's mth frame may differ from SV to SV and frame to frame at both the CS and CT, which influences the variance of $w(i,m)$ over time. Second, the shared CT clock parameters between measurements introduce correlation.

To begin, we first assume that the SNR for the ith satellite remains relatively constant for the entire FAI, as observed at both the CS and the CT. Therefore, we can define $w(i,m) \approx w(i) \sim \mathcal{N}(0, \sigma^2(i)), m \in \mathcal{M}_i$. The measurement covariance matrix of the ith SV $R_a(i) = \sigma_\rho^2(i)\mathbb{I}_i$, where $\mathbb{I}_i$ is the identity matrix with size equal to the cardinality of $\mathcal{M}_i$. Consequently, the measurement covariance matrix for all SVs, due to TOA estimation error is then the block diagonal matrix

$$R_a = \begin{bmatrix} R_a(0) & 0 & \dots & 0 \\ 0 & R_a(1) & \dots & 0 \\ \vdots & \vdots & \ddots & \vdots \\ 0 & 0 & \dots & R_a(n-1) \end{bmatrix} \tag{42}$$

where each 0 is an appropriately sized matrix of all zeros.

To address the clock errors, we first point to the original measurement model in (21). Dropping the FAI index, the CT clock offset term $\delta t_{\text{u}}(i,m)$ is a random variable, which is modeled as a combination of a Wiener process and an integrated Wiener process [46]. It's instantaneous variance is given by $\sigma^2_{\delta t_{\text{u}}}(i,m) = S_f\Delta t(i,m) + \frac{S_g\Delta t^3(i,m)}{3}$ in [47], where $S_f = \frac{h_0}{2}$ and $S_g = 2\pi^2 h_{-2}$ are the power spectral densities of the phase and frequency random processes of the receiver clock, respectively. Typically, the coefficients h_0 and h_{-2} are determined through laboratory experiments.

The measurement covariance matrix introduced by the clock offset random process is determined as follows. For the receiver clock offset at the time of the ith and jth SV's mth and kth frames, respectively the covariance is

$$\begin{aligned}\mathbb{E}[\delta t_{\text{u}}(i,m)\delta t_{\text{u}}(j,k)] = S_f\Delta t_{\text{m}} + \frac{S_g\Delta t_{\text{m}}^3}{3} \\ \text{where} \quad \Delta t_{\text{m}} = \min(\Delta t(i,m), \Delta t(j,k))\end{aligned} \tag{43}$$

Therefore, we may define each element of the measurement covariance due to CT clock errors R_{clk} as in (43). As a simple example, consider the 3×3 case where three TOA measurements are extracted from three frames from two SVs. Then, R_{clk} would be

$$R_{\text{clk}} = \begin{bmatrix} \sigma^2_{\delta t_{\text{u}}}(0,0) & \sigma^2_{\delta t_{\text{u}}}(0,0) & \sigma^2_{\delta t_{\text{u}}}(0,0) \\ \sigma^2_{\delta t_{\text{u}}}(0,0) & \sigma^2_{\delta t_{\text{u}}}(1,0) & \sigma^2_{\delta t_{\text{u}}}(1,0) \\ \sigma^2_{\delta t_{\text{u}}}(0,0) & \sigma^2_{\delta t_{\text{u}}}(1,0) & \sigma^2_{\delta t_{\text{u}}}(1,1) \end{bmatrix} \tag{44}$$

From there, it is straightforward to extrapolate R_{clk} for multiple TOA measurements from various satellites and frames.

Then, the final measurement covariance matrix R is formed as

$$R = R_a + c^2 R_{\text{clk}} \tag{45}$$

C. Maximum a Posteriori Least Squares Update

At this point, the weighted NBLS estimator would allow the states $\boldsymbol{\delta\eta}$ to explore any value. However, since we have *a priori* information about the distributions of $\boldsymbol{\delta\eta}$, we can incorporate this information within the NBLS update step as follows. First, consider the traditional weighted NBLS update step at the kth iteration with residuals $\boldsymbol{\delta z}$

$$\hat{\boldsymbol{x}}_k = \hat{\boldsymbol{x}}_{k-1} + (H^\mathsf{T} R^{-1} H)^{-1} H^\mathsf{T} R^{-1} \boldsymbol{\delta z} \tag{46}$$

We may apply the *a priori* distribution of $\hat{\boldsymbol{x}}_0$ to the update, assuming that $\hat{\boldsymbol{x}}_0 \sim \mathcal{N}(\boldsymbol{x}_0, P)$. The update step then becomes

$$\hat{\boldsymbol{x}}_k = \hat{\boldsymbol{x}}_{k-1} + (H^\mathsf{T} R^{-1} H + P^{-1})^{-1} (H^\mathsf{T} R^{-1} \delta \boldsymbol{z} + P^{-1} \boldsymbol{\delta x}) \tag{47}$$

where $\boldsymbol{\delta x} = \hat{\boldsymbol{x}}_{k-1} - \boldsymbol{x}_0$, and $\boldsymbol{x}_0$ is the initial guess of the iterative NBLS process. Assuming no prior knowledge of the position, clock offset, or clock drift states, the *a priori* covariance matrix $P \in \mathbb{R}^{5+n-1}$ will be diffuse for the first four states and the final state. Said differently, the first four diagonal elements of P and the last diagonal element of P will be set to ∞ to reflect a complete lack of prior knowledge. The elements corresponding to the $\boldsymbol{\delta\eta}$ states will be set to P_η and the elements corresponding to the covariance between $\boldsymbol{\delta\eta}$ and the diffuse states will be set to 0.

The matrix P_η is defined using the distributions derived in Section VI. To define P_η in this way, we first make the simplification that $\eta(i) \sim \mathcal{N}(0, \bar{\sigma}_\eta^2(i)), i \in \mathcal{I}$, where $\mathcal{I}$ is the set of all SVs used in the NBLS estimator. After making this simplification, we can recognize that

$$\boldsymbol{\delta\eta} \sim \mathcal{N}(\mathbf{0}, P_\eta) \tag{48}$$

$$P_\eta = \begin{bmatrix} \bar{\sigma}_\eta^2(0) + \bar{\sigma}_\eta^2(1) & \bar{\sigma}_\eta^2(0) & \dots & \bar{\sigma}_\eta^2(0) \\ \bar{\sigma}_\eta^2(0) & \bar{\sigma}_\eta^2(0) + \bar{\sigma}_\eta^2(2) & \dots & \bar{\sigma}_\eta^2(0) \\ \vdots & \vdots & \ddots & \vdots \\ \bar{\sigma}_\eta^2(0) & \bar{\sigma}_\eta^2(0) & \dots & \bar{\sigma}_\eta^2(0) + \bar{\sigma}_\eta^2(n-1) \end{bmatrix} \tag{49}$$

Then, the initial guess is set to $\boldsymbol{x}_0 = \begin{bmatrix} \boldsymbol{p}_0 & \mathbf{0} \end{bmatrix}^\mathsf{T}$, where $\boldsymbol{p}_0$ is some diffuse initial position guess, and $\mathbf{0}$ is the zero vector of length $n+1$. From there, given a set of measurements $\boldsymbol{z}$ the CT may form a solution using the weighted NBLS estimator by iteratively applying (47) over a predefined number of iterations or until the second quantity in (47) becomes sufficiently small.

VIII. Experimental Results

This section discusses the experiment we devised to test our mock implementation of fused LEO GNSS, including the signal capture setup, the specific scenario, and the results obtained.

A. Signal Capture

To capture signal data, a CS receiver and a CT receiver were set up. The CS was located on the roof of the Aerospace Engineering Building on the University of Texas campus. The CS used a steerable 90-cm offset parabolic dish with an approximately 3 degree beamwidth to receive Starlink signals. The dish was steered to desired SVs using TLEs, with the beamwidth limiting captures to a single SV at a time. The parabolic dish was equipped with a feedhorn connected to a low-noise block (LNB), which has a conversion gain of 60 dB and a noise figure of 0.8 dB. The LNB downconverts 10.7–11.7 GHz signals to 950–1950 MHz, or 11.7–12.75 GHz to 1100–2150 MHz. The antenna's nominal gain is 40 dBi at 12.5 GHz, with at least 4-5 dB of losses due to the absence of a circular-to-linear polarizer and feedhorn misalignment.

The CS also featured a signal capture system capable of continuous sampling at 250 Msps. The usable bandwidth of the capture is around 200 MHz, which was ample to obtain high-quality TOAs from Starlink's $F_\text{s} = 240$ MHz Ku-band downlink signal. The hardware then performed downmixing to baseband, bandpass filtering, and 16-bit complex sampling. The capture system can simultaneously capture on two channels, with the limitation that the sampling rate must be identical for both channels to start sampling simultaneously. This setup is referred to as a dual capture. To extract TOTs as described in [26], a dual capture of both Starlink and GNSS data was performed for all captures treated in this paper. The signal capture system and the LNB local oscillators were both driven by an external GPS disciplined oven-controlled crystal oscillator (GPSDO).

The CT was located in the parking lot of the Whitaker tennis courts in Austin, TX, approximately 3.009 km from the CS. The CT used the same feedhorn and LNB as the CS, but did not have a parabolic dish. Instead, the CT faced the feedhorn directly towards zenith to collect data. The CT also featured a signal capture system. It was only capable of continuous sampling at 25 Msps. The hardware performed the same steps as in the CS, including downmixing to baseband, bandpass filtering, and 16-bit complex sampling. Like the CS, the CT's signal capture system can also perform a dual capture. For ground truth, a dual capture of both Starlink and GNSS data was performed at the CT as well. Since the CS and CT were only able to observe one SV at a time, there were often long gaps between observations. To make long gaps appear short, the CT signal capture system's local oscillator was also driven by an external GPSDO, and the LNB's local oscillator was driven by the same GPSDO.

B. Scenario Description

Starlink signal data was recorded over approximately a 13-minute period in January 2025. During this time, the CT was continuously capturing to ensure local clock coherence between SVs. The CS sporadically captured as SVs became observable, capturing data in 60-second periods. Both the CS and the CT captured data at a center frequency of 12.075 GHz, corresponding to channel 6 from [29]. Over this period, 5 SVs were visible. Fig. 6 shows the ground tracks of the recorded

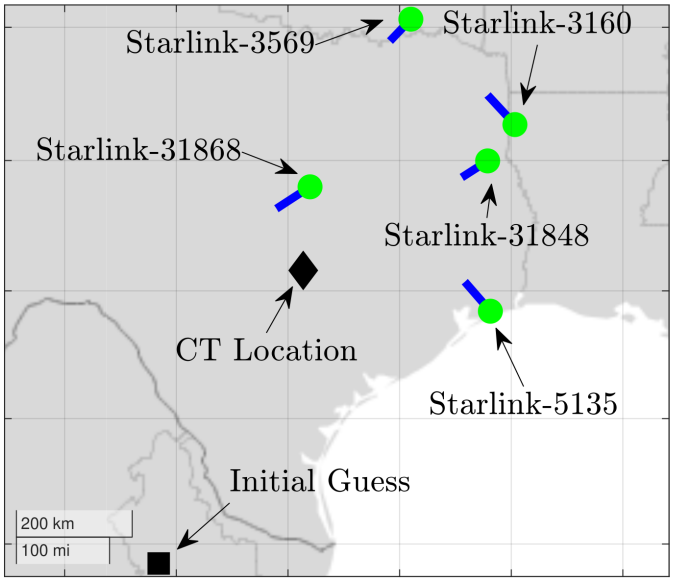

Fig. 6: The ground tracks of the recorded Starlink SVs. In total, 5 SVs were recorded, with identifiers, in order of capture, being 5135, 31686, 3160, 3569, and 31848. The black diamond marks the location of the CT and the black square marks the location of the NBLS initialization.

Starlink SVs. For all 5 SVs, measurements were generated over a 10-second period during an FAI. The gaps between SVs ranged from as few as 100 seconds and as many as 280 seconds.

TOA measurements were made at the CT by using full frames as local replicas. Since Starlink frames change frequently and the modulation of each symbol in each frame also changes, sometimes within a symbol (as shown in [42]), decoding enough frames to generate a significant number of measurements proved too cumbersome. Instead, we opted to directly correlate the CS in-phase and quadrature samples with those of the CT. This process is similar to the *decision-directed* approach described in Section V. We acknowledge that this is a suboptimal method to extract these measurements, and improvements could be made in the future. In total, $N_z = 6384$ TOA measurements were extracted from 5 SVs over 50 seconds of data. The measurements from a single SV are spaced at arbitrary multiples of the frame rate $1/750$ seconds.

For these data, only TLEs were available. Most of the TLEs were 24 hours old, with one being just 12 hours old. We determined P_η from Section VII-C by using the method described in Section VI-B. To do this, we assumed that the position of the CT was Gaussian distributed with $\sigma_e = \sigma_n = 3.3$ km and $\sigma_u = 50$ m around the CS. Since the TLEs were around 24 hours old, $\sigma_{\text{eph}} = 5$ km was used. Given that the CT's local oscillator was driven by a GPSDO, we set $h_0 = 5 \times 10^{-23}$ and $h_{-2} = 3 \times 10^{-26}$ to model an especially good OCXO.

C. Results

The NBLS estimator was set up as in Section VII and initialized in Monterrey, MX, as shown in Fig. 6, approximately 572 km away from the CT. Fig. 7 plots the results of the NBLS using the measurements obtained during our field experiment. At the top, the residuals are shown. The residuals are nearly zero-mean and show the long gaps between SV observations. The final solution is plotted below the residuals. The solution has an absolute 3D error of 6.47 m, with a 95% confidence ellipse that has a semi-major axis of 11.96 m and a semi-minor axis of 6.31 m. The reported altitude has a 95% confidence interval of ± 18.6 m around its solution. Finally, the clock offset state δt_η is resolved within a 95% confidence interval of ± 17.29 m around its solution. Considering that this estimate is the combination of the true clock offset $\delta t_u(0,0)$ and the TLE error $\eta(0)$, we can incorporate the distribution of $\eta(0)$ into the confidence interval for resolving the true clock offset. Assuming a 24 hour old TLE, the confidence interval expands to ± 73.27 m around the true clock offset. Converting to seconds this allows us to resolve clock offset to ± 244.39 ns with 95% confidence.

IX. Conclusion

In this paper we presented a method for producing a pseudorange-based PNT solution using Starlink's Ku-band downlink signal. We tested this method in a field campaign and achieved 10-meter-level position and timing accuracy, despite challenges presented by large ephemeris errors, a low-gain receiver antenna, and a narrow-bandwidth front-end. SpaceX could readily implement a full-fledged fused LEO GNSS service using the methods described here. The accuracy of such a service would exceed what we have demonstrated, provided that SpaceX has access to meter-accurate ephemeris data for their Starlink SVs and could actively monitor their SV clocks to within $\sim$10 ns. Alternatively, a third-party service could be developed, deploying reference stations at service-cell density to provide timing and ephemeris corrections to users. In either case, we believe that the present work establishes the viability of pseudorange-based LEO PNT as a backup to traditional GNSS in the near term. Looking further ahead, we expect LEO PNT to eventually provide PNT services superior to traditional GNSS.

Acknowledgments

Research was supported by the U.S. Department of Transportation under Grant 69A3552348327 for the CARMEN+ University Transportation Center, and by affiliates of the 6G@UT center within the Wireless Networking and Communications Group at The University of Texas at Austin.

References

[1] O. Kutkov, "Connecting external GPS antenna to the starlink terminal," https://olegkutkov.me/2023/11/07/connecting-external-gps-antenna-to-the-starlink-terminal/, 2023, accessed: 2023-03-01.

[2] T. G. Reid, A. M. Neish, T. Walter, and P. K. Enge, "Broadband LEO constellations for navigation," *NAVIGATION*, vol. 65, no. 2, pp. 205–220, 2018.

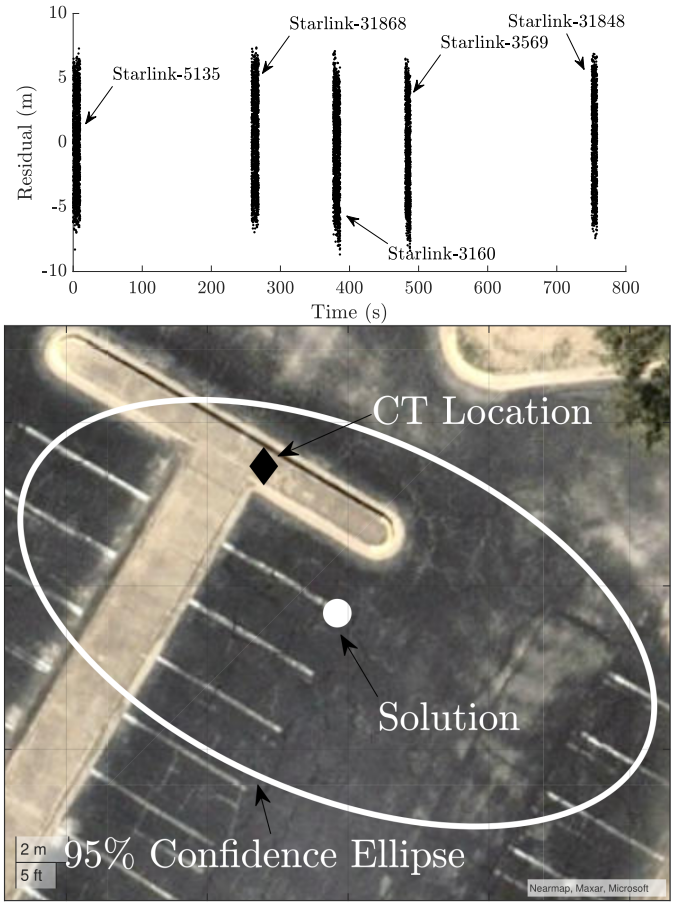

Fig. 7: The post-fit residuals from the NBLS estimator (top). The residuals are fairly zero-mean. Also plotted is the NBLS position solution, marked with a white circle, alongside the true location of the CT, marked with a black diamond. The solution has an absolute 3D error of 6.47 m, with a 95% confidence ellipse that has a semi-major axis of 11.96 m and a semi-minor axis of 6.31 m.

[3] F. S. Prol, R. M. Ferre, Z. Saleem, P. Valisuo, C. Pinell, E. S. Lohan, M. Elsanhoury, M. Elmusrati, S. Islam, K. Celikbilek, K. Selvan, J. Yliaho, K. Rutledge, A. Ojala, L. Ferranti, J. Praks, M. Z. H. Bhuiyan, S. Kaasalainen, and H. Kuusniemi, "Position, navigation, and timing (PNT) through low earth orbit (LEO) satellites: A survey on current status, challenges, and opportunities," *IEEE access*, vol. 10, pp. 83 971–84 002, 2022.

[4] T. E. Humphreys, "Interference," in *Springer Handbook of Global Navigation Satellite Systems*. Springer International Publishing, 2017, pp. 469–503.

[5] M. J. Murrian, L. Narula, P. A. Iannucci, S. Budzien, B. W. O'Hanlon, M. L. Psiaki, and T. E. Humphreys, "First results from three years of GNSS interference monitoring from low Earth orbit," *NAVIGATION*, vol. 68, no. 4, pp. 673–685, 2021.

[6] Z. Clements, P. Ellis, and T. E. Humphreys, "Dual-satellite geolocation of terrestrial GNSS jammers from low Earth orbit," in *Proceedings of the IEEE/ION PLANS Meeting*, Monterey, CA, 2023, pp. 458–469.

[7] G. S. Workgroup, "GPS spoofing: Final report of the GPS spoofing workgroup," OPSGROUP, Tech. Rep., 2024. [Online]. Available: https://ops.group/blog/gps-spoofing-final-report

[8] Z. L. Clements, P. B. Ellis, M. J. Murrian, M. L. Psiaki, and T. E. Humphreys, "Single-satellite-based geolocation of broadcast GNSS spoofers from low Earth orbit," *NAVIGATION*, 2025, submitted for review.

[9] W. Van Uytsel, T. Janssen, M. Weyn, and R. Berkvens, "A technical overview of current "new space" LEO-PNT initiatives and their application potential," in *2024 IEEE 35th International Symposium on Personal, Indoor and Mobile Radio Communications (PIMRC)*. IEEE, 2024, pp. 1–6.

[10] E. Rubinov, "FrontierSI State of the Market Report LEO PNT 2024 Edition," Jan. 2025, https://frontiersi.com.au/wp-content/uploads/2025/01/FrontierSI-State-of-Market-Report-LEO-PNT-2024-Edition-v1.1.pdf.

[11] N. S. Miller, J. T. Koza, S. C. Morgan, S. M. Martin, A. Neish, R. Grayson, and T. Reid, "SNAP: A Xona Space Systems and GPS software-defined receiver," in *2023 IEEE/ION Position, Location and Navigation Symposium (PLANS)*. IEEE, 2023, pp. 897–904.

[12] P. A. Iannucci and T. E. Humphreys, "Fused low-Earth-orbit GNSS," *IEEE Transactions on Aerospace and Electronic Systems*, pp. 1–1, 2022.

[13] ——, "Economical fused LEO GNSS," in *Proceedings of the IEEE/ION PLANS Meeting*, 2020.

[14] A. M. Graff and T. E. Humphreys, "Ziv-Zakai-optimal OFDM resource alocation for time-of-arrival estimation," *IEEE Transactions on Wireless Communications*, 2025.

[15] ——, "OFDM-based positioning with unknown data payloads: Bounds and applications to LEO PNT," *IEEE Transactions on Wireless Communications*, 2024, submitted for review.

[16] Z. M. Kassas, N. Khairallah, and S. Kozhaya, "Ad astra: Simultaneous tracking and navigation with megaconstellation LEO satellites," *IEEE Aerospace and Electronic Systems Magazine*, 2024.

[17] S. Shahcheraghi, J. Saroufim, and Z. M. Kassas, "Acquisition, Doppler tracking, and differential LEO-aided IMU navigation with uncooperative satellites," *IEEE Transactions on Aerospace and Electronic Systems*, 2025.

[18] J. Saroufim and Z. M. Kassas, "Ephemeris and timing error disambiguation enabling precise LEO PNT," *IEEE Transactions on Aerospace and Electronic Systems*, 2025.

[19] S. Zhou, R. Yang, Y. Li, X. Zhan, and H. Qin, "Iridium TOA estimation and positioning based on carrier tracking and beam decoding," *IEEE Transactions on Instrumentation and Measurement*, vol. 74, pp. 1–23, 2025.

[20] Z. M. Komodromos, S. C. Morgan, Z. L. Clements, W. Qin, W. J. Morrison, and T. E. Humphreys, "Network-aided pseudorange-based LEO PNT from OneWeb," in *Proceedings of the IEEE/ION PLANS Meeting*, Salt Lake City, UT, 2025.

[21] Z. Tan, H. Qin, L. Cong, and C. Zhao, "Positioning using IRIDIUM satellite signals of opportunity in weak signal environment," *Electronics*, vol. 9, no. 1, p. 37, 2019.

[22] M. L. Psiaki, "Navigation using carrier Doppler shift from a LEO constellation: TRANSIT on steroids," *NAVIGATION*, vol. 68, no. 3, pp. 621–641, 2021.

[23] M. Neinavaie, J. Khalife, and Z. M. Kassas, "Acquisition, Doppler tracking, and positioning with Starlink LEO satellites: First results," *IEEE Transactions on Aerospace and Electronic Systems*, vol. 58, no. 3, pp. 2606–2610, 2022.

[24] B. McLemore and M. L. Psiaki, "Navigation using Doppler shift from LEO constellations and INS data," *IEEE Transactions on Aerospace and Electronic Systems*, vol. 58, no. 5, pp. 4295–4314, 2022.

[25] N. Jardak, R. Adam, and Q. Jault, "Leveraging multi-LEO satellite signals for opportunistic positioning," *IEEE Access*, 2024.

[26] W. Qin, A. M. Graff, Z. L. Clements, Z. M. Komodromos, and T. E. Humphreys, "Timing properties of the Starlink Ku-band downlink," *IEEE Transactions on Aerospace and Electronic Systems*, 2025, submitted for review.

[27] H. Sallouha, S. Saleh, S. De Bast, Z. Cui, S. Pollin, and H. Wymeersch, "On the ground and in the sky: A tutorial on radio localization in ground-air-space networks," *IEEE Communications Surveys and Tutorials*, vol. 27, no. 1, pp. 218–258, 2025.

[28] A. Baron, P. Gurfil, and H. Rotstein, "Implementation and accuracy of Doppler navigation with LEO satellites," *NAVIGATION: Journal of the Institute of Navigation*, vol. 71, no. 2, 2024.

[29] T. E. Humphreys, P. A. Iannucci, Z. M. Komodromos, and A. M. Graff, "Signal structure of the Starlink Ku-band downlink," *IEEE Transactions on Aerospace and Electronic Systems*, pp. 1–16, 2023.

[30] Z. M. Komodromos, W. Qin, and T. E. Humphreys, "Weak signal acquisition and tracking of the Starlink Ku-Band downlink to enable global PNT," in *Proceedings of the ION Joint Navigation Conference (JNC)*, 2024.

[31] T. Fan, T. Zhang, H. Zhang, J. Mo, and X. Niu, "A double sideband combined tracking method for Galileo E5 AltBOC signals," *Satellite Navigation*, vol. 4, no. 1, p. 27, 2023.

[32] S. Pekhterev, "The bandwidth of the Starlink constellation and the assessment of its potential subscriber base in the USA," *SatMagazine*, vol. 11, pp. 54–57, 2021.

[33] W. Qin, Z. M. Komodromos, and T. E. Humphreys, "An agile, portable antenna system for LEO megaconstellation-based PNT," in *Proceedings of the ION GNSS+ Meeting*, 2023.
[34] G. Huston, "A transport protocol's view of Starlink," May 2024, accessed: 2024-11-22. [Online]. Available: https://blog.apnic.net/2024/05/17/a-transport-protocols-view-of-starlink/
[35] N. Mohan, A. E. Ferguson, H. Cech, R. Bose, P. R. Renatin, M. K. Marina, and J. Ott, "A multifaceted look at Starlink performance," in *Proceedings of the ACM on Web Conference 2024*, 2024, pp. 2723–2734.
[36] E. Grayver, R. Nelson, E. McDonald, E. Sorensen, and S. Romano, "Position and navigation using Starlink," in *2024 IEEE Aerospace Conference*. IEEE, 2024, pp. 1–12.
[37] O. Montenbruck, A. Hauschild, and P. Steigenberger, "Differential code bias estimation using multi-GNSS observations and global ionosphere maps," *NAVIGATION*, vol. 61, no. 3, pp. 191–201, 2014.
[38] M. Meurer and F. Antreich, "Signals and modulation," in *Springer Handbook of Global Navigation Satellite Systems*. Springer International Publishing, 2017, pp. 91–119.
[39] C. Jekeli and O. Montenbruck, "Time and reference systems," in *Springer Handbook of Global Navigation Satellite Systems*. Springer International Publishing, 2017, pp. 25–58.
[40] R. Beard and K. Senior, "Clocks," in *Springer Handbook of Global Navigation Satellite Systems*. Springer International Publishing, 2017, pp. 121–164.
[41] M. Skolnik, *Introduction to radar systems 2nd Edition*. McGraw-Hill, 1980.
[42] W. Qin, Z. M. Komodromos, S. C. Morgan, and T. E. Humphreys, "Maximum likelihood time of arrival and Doppler estimation for precise Starlink-based PNT," in *Proceedings of the IEEE/ION PLANS Meeting*, Salt Lake City, UT, 2025.
[43] A. Liu, X. Xu, Y. Xiong, and S. Yu, "Maneuver strategies of Starlink satellite based on SpaceX-released ephemeris," *Advances in Space Research*, 2024.
[44] J. R. Vetter, "Fifty years of orbit determination," *Johns Hopkins APL technical digest*, vol. 27, no. 3, p. 239, 2007.
[45] Z. Clements, P. Ellis, M. L. Psiaki, and T. E. Humphreys, "Geolocation of terrestrial GNSS spoofing signals from low Earth orbit," in *Proceedings of the ION GNSS+ Meeting*, Denver, CO, 2022, pp. 3418–3431.
[46] L. Galleani, "A tutorial on the two-state model of the atomic clock noise," *Metrologia*, vol. 45, no. 6, p. S175, 2008.
[47] R. G. Brown and P. Y. Hwang, *Introduction to Random Signals and Applied Kalman Filtering*. Wiley, 2012.